Journal of Materials Science & Technology 108 (2022) 226–235

Contents lists available at ScienceDirect

Journal of Materials Science & Technology

journal homepage: www.elsevier.com/locate/jmst

Research Article

Achieving superior mechanical properties of selective laser melted AlSi10Mg via direct aging treatment

H. Zhang[a], Y. Wang[a,b], J.J. Wang[b], D.R. Ni[a,*], D. Wang[a], B.L. Xiao[a,*], Z.Y. Ma[a]

[a] Shi-changxu Innovation Center for Advanced Materials, Institute of Metal Research, Chinese Academy of Sciences, 72 Wenhua Road, Shenyang 110016, China

[b] College of Materials Science and Engineering, Shenyang Aerospace University, 37 Daoyi South Avenue, Shenyang 110136, China

ARTICLE INFO

Article history:
Received 27 February 2021
Revised 18 July 2021
Accepted 22 July 2021
Available online 29 October 2021

Keywords:
Additive manufacturing
Selective laser melting
AlSi10Mg alloy, Heat treatment

ABSTRACT

For additive manufactured aluminum alloys, the inferior mechanical properties along the building direction have been a serious weakness. In this study, an optimized heat treatment was developed as a simple and effective solution. The effects of direct aging on microstructure and mechanical properties along the building direction of AlSi10Mg samples produced via selective laser melting (SLM) were investigated. The results showed that, compared with the conventional heat treatment at elevated temperatures, direct aging at temperatures of 130–190 °C could retain the fine grain microstructure of SLM samples and promote further precipitation of Si phase, however, the growth of pores occurred during direct aging. With increasing aging temperature, while finer cell structures were obtained, more and larger pores were developed, resulting in decreased density of the samples. Two types of pore formation mechanisms were identified. Considering the balance between the refinement of cell structure and the growth of pores, aging at 130 °C was determined as the optimized heat treatment for SLM AlSi10Mg samples. The tensile strength along the building direction of the 130 °C aged sample was increased from 403 MPa to 451 MPa, with relatively high elongation of 6.5%.

1. Introduction

Recently, with the urgent demands of intelligent manufacturing, personalized production, and lightweight structure design, 3D printing technology has been developed rapidly [1–5]. Selective laser melting (SLM), as one of the most promising 3D printing technologies, has attained massive attention due to its high designability and manufacturing accuracy [6–11]. Nowadays, SLM has been used to produce complex components in high-tech industry fields, such as aerospace, shipbuilding, and automotive [12–17]. Aluminum alloys, nickel alloys, steels, and titanium alloys are mainly selected for SLM.

AlSi10Mg is a widely used casting alloy that possesses good castability and weldability, high thermal conductivity (113 W/(m K) [18]), relatively high corrosion resistance, heat resistance and abrasion resistance. More importantly, the isothermal solidification character makes AlSi10Mg an ideal material for 3D printing with little cracking tendency. Compared to those by traditional sand mold casting and high-pressure casting, the mechanical properties of AlSi10Mg alloy prepared by SLM have been significantly improved [19,20].

For structural materials and engineering parts, the overall performance highly depends on the weakest zones. Because of the layer by layer stacking mode and the complex thermal cycle history, the SLM samples generally exhibit an inhomogeneous microstructure in the building direction, resulting in inferior mechanical properties [20,21]. To obtain homogeneous microstructure and to improve the mechanical properties along the building direction, the effects of heat treatments on the properties of the SLM samples have been investigated [9,20–27]. Stress relief annealing and T6 heat treatment (solid solution treatment and subsequent artificial aging) are commonly selected for the SLM Al alloys [21,26–28].

It has been reported that, although the stress relief annealing at 300 °C improved elongation of the SLM samples, the strength was decreased significantly [9]. High temperature solid solution heat-treatment also deteriorated the hardness of the SLM samples due to grain growth [26]. Clearly, although the T6 and annealing heat-treatments are suitable for conventional casting aluminum alloys, they are not the optimal heat-treatment methods for fine-structured SLM samples.

Since the cooling rate of the molten pool during SLM is exceptionally high (10^3–10^5 °C/s) [29], the SLM samples generally possess a fine supersaturated microstructure. To take full advantage of the effects of solid-solution strengthening and fine-grain

* Corresponding authors.
E-mail addresses: drni@imr.ac.cn (D.R. Ni), blxiao@imr.ac.cn (B.L. Xiao).

https://doi.org/10.1016/j.jmst.2021.07.059
1005-0302/

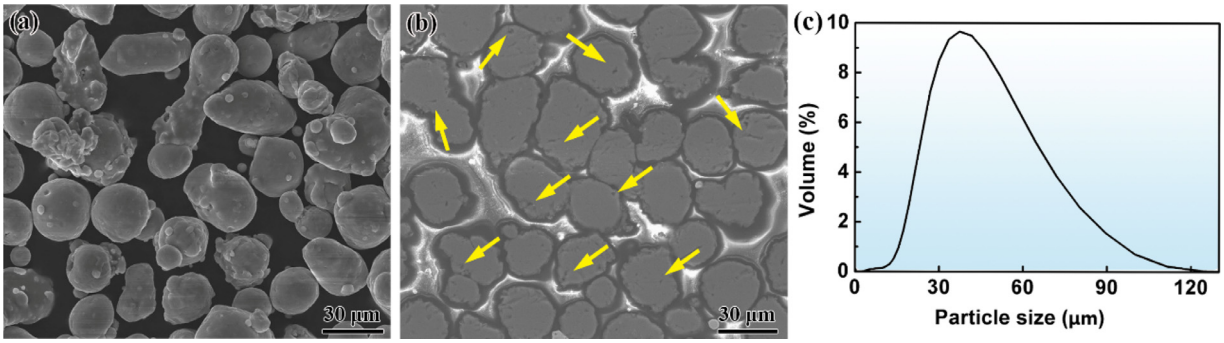

Fig. 1. (a) AlSi10Mg powders, (b) internal morphology (the arrows indicate pores inside the powders), and (c) particle size distribution.

strengthening, the temperature and holding time of heat treatment for the SLM samples should be strictly controlled. In this case, direct aging might be a feasible method. Kempen et al. [19] pointed out that, after direct aging at 175 °C for 6 h, the hardness of SLM AlSi10Mg samples increased from 136 HV to 152 HV, and the strength and elongation were basically unchanged (396 MPa vs. 399 MPa, 3.5% vs. 3.3%). Casati et al. [21] reported that, after direct aging at 160 °C, the SLM AlSi10Mg sample showed a high strength of 493 MPa and acceptable elongation of 6% along the building direction, however, no comparison of strength between aged and as-built samples was made.

From the limited results above, it can be deduced that, for the SLM samples, the temperature of direct aging plays a very important role. The mechanical properties of lower temperature aged samples might be better. Rosenthal et al. [22] and Fiocchi et al. [30] pointed out that, for the SLM samples with refined microstructure, the heat treatment temperature should be reduced accordingly. However, the aging temperatures in the previous studies were selected based on the traditional heat treatment processes, and the effects of aging temperatures on the microstructural evolution and mechanical properties of the SLM samples were not investigated. Therefore, it is highly desirable to explore the optimized aging temperature to further improve the mechanical properties of the SLM AlSi10Mg samples.

Furthermore, Delahaye et al. [31] found that, the fracture of the SLM samples along the building direction generally occurred in the heat-affected zone (HAZ) due to lower hardness. Thus, the key to eliminate the weakness of the SLM samples is to improve the strength of the HAZ. Due to the fine supersaturated microstructure of the SLM samples [21,32], the further precipitation of secondary phases in the HAZ during aging can be a simple and effective solution.

With low temperature direct aging, the defect growth mechanism within the SLM samples can be very different, high defect density will impede the improvement of strength and ductility of the SLM samples. However, the existing studies mainly focused on the defect formation during SLM and T6 heat treatment. The effects of aging parameters on the defect growth are still unknown.

In this study, the SLM AlSi10Mg samples were subjected to aging treatment at various temperatures. The aims are to (a) optimize the aging temperature and (b) clarify the mechanism of strength improvement along the building direction and defect growth during aging treatment for SLM AlSi10Mg samples.

2. Materials and methods

2.1. SLM process and aging treatment

AlSi10Mg powders were provided by Renishaw with a chemical composition of Al-9.8Si-0.45Mg-0.25Fe (in wt.%). As-received powders exhibited an ellipsoidal shape with an average size of ~43 μm (Fig. 1), a few small pores could be found inside the powders. Renishaw AM400 SLM system was used to fabricate cuboid samples (10 × 10 × 70 mm). As shown in Fig. 2, X refers to the direction of the scraper movement; Z indicates the building direction. The rotation angle between each adjacent layer was set to 67° to avoid overlap between layers. The printing parameters are shown in Table 1.

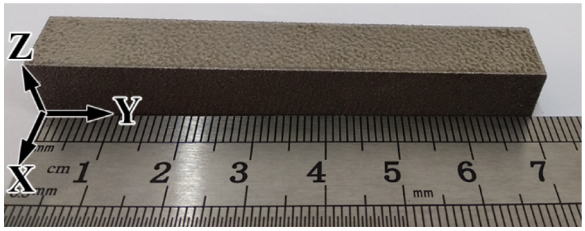

Fig. 2. AlSi10Mg samples produced by SLM.

Table 1
. Parameters for SLM processing and heat treatment.

Parameters	Value
Laser power	275 W
Scanning speed	1.6 m/s
Layer thickness	30 μm
Average particle size	43 μm
Aging temperature	130/150/170/190 °C (4 h)

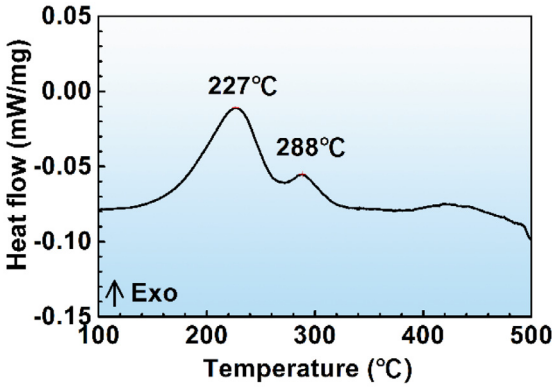

Fig. 3. DSC profile of SLM AlSi10Mg sample.

Precipitation analysis was carried out using differential scanning calorimetry (DSC, TA-Q1000 system) under argon atmosphere from 100 °C to 500 °C with a heating rate of 5 °C/min. According to the result in Fig. 3, the specimens were heat-treated under aging temperatures from 130 °C to 190 °C for 4 h, as shown in Table 1.

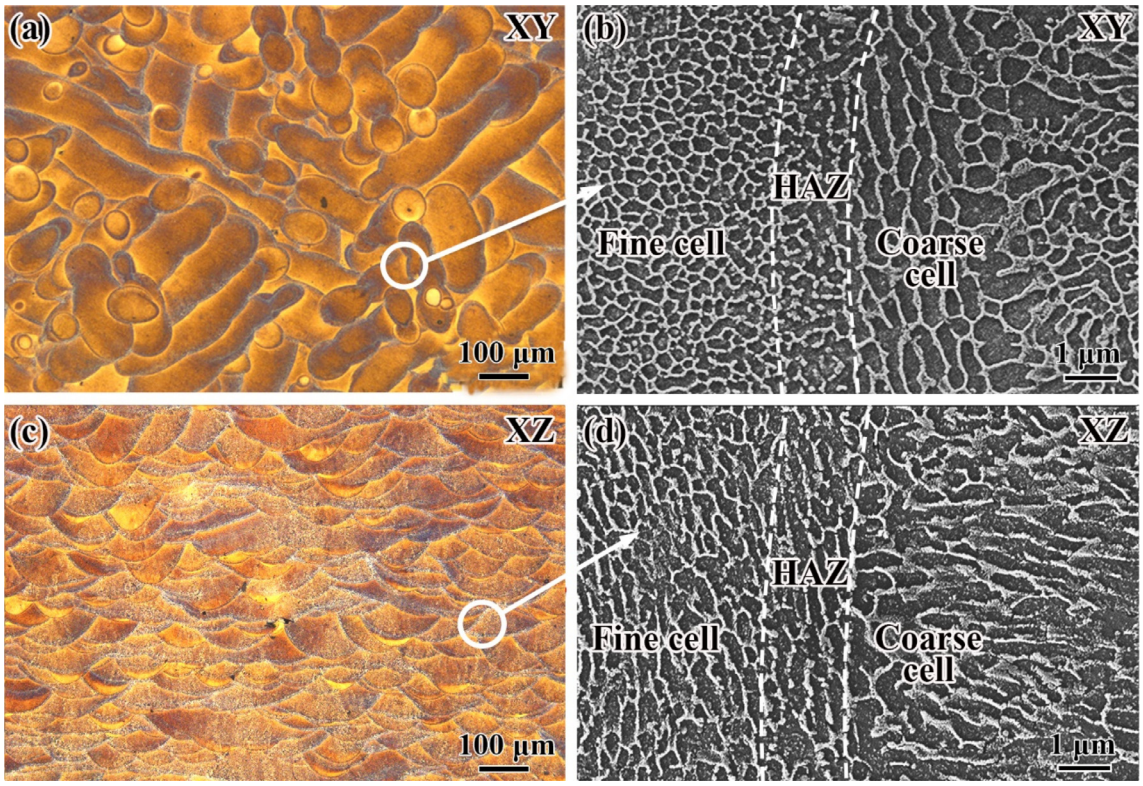

Fig. 4. Microstructure of as-fabricated AlSi10Mg samples on (a, b) horizontal and (c, d) building sections.

2.2. Microstructure characterization

For microstructure and phase analysis, the samples were ground and mechanically polished, then etched with Keller's reagent (190 ml distilled water, 5 ml HNO_3, 3 ml HCl, 2 ml HF) for 60 s. Optical microscopy (OM, Zeiss Axiovert 200 MAT) and field emission scanning electron microscopy (FESEM, Leo Supra 55) were used for the microstructural examination. Transmission electron microscopy (TEM, FEI Tecnai F20, and FEI Tecnai Spirit TEM T12) observation was conducted and the samples were prepared with Gatan 695 ion-miller. Scanning transmission electron microscopy (STEM) and X-ray energy-dispersive spectroscopy (EDS) were used to analyze the phase and element distribution.

2.3. Mechanical tests

The tensile samples with a gage size of 5 mm × 1.4 mm × 1.2 mm were cut parallel to the building direction. Tensile tests were conducted using Instron 8801 with a strain rate of 1×10^{-3} s^{-1} at room temperature. Vickers hardness was measured by FM-700 microhardness testing machine with a 50 g load and 10 s dwell time. To compare the hardness changes near the molten pool boundaries before and after aging treatment, a lower load of 10 g was selected.

3. Results

3.1. Microstructural evolution

3.1.1. Macrostructure and molten pool morphology

The macrostructure of the horizontal and vertical sections of the as-fabricated sample is shown in Fig. 4. As observed in Fig. 4(a) and (c), near fully dense sample with a typical stacking morphology was obtained. Fig. 4(c) reveals the shape of the molten pool along the building direction. As can be observed, the depth of the molten pool was ~59 μm, while the width was ~130 μm. Within the molten pool, the Al-Si eutectic phase was observed. Due to the extremely high thermal gradient during SLM, inhomogeneous microstructure was formed [29]. The molten pool could be divided into three zones according to the morphologies: fine cell zones (mean diameter: 0.82 μm), coarse cell zones, and HAZ with broken Si network (Fig. 4(b) and (d)). Similar results have been reported by Thijs et al. [14].

As shown in Fig. 5, after aging at different temperatures, significant microstructural changes could be observed. Firstly, with the elevation of the aging temperature, the width of broken Si network in the HAZ decreased from 1.8 μm to 0.5 μm, as shown in Figs. 4d and Fig. 5, leading to a more homogeneous microstructure. Secondly, the area fraction of Si network increased significantly after aging. For 190 °C aged sample, the statistical data indicated that the total Si network area fraction increased from 32.6% to 49.7%. At the same time, the cell structure was significantly refined, the mean diameter of the fine-cells was about 0.75 μm at 130 °C and decreased to 0.34 μm after aging at 190 °C (measured by the mean linear intercept method, Fig. 5). Thirdly, precipitates with various shapes within the cells were observed. In Fig. 5(b)–(d), the spheroidization of the Si precipitates could be observed with the increasing aging temperature.

3.1.2. Density and porosity

In general, the mechanical properties of the SLM samples highly depend on their microstructure and density [19,33]. After 130 °C aging, the number of the pores increased (Fig. 6(a) and (b)). With higher aging temperatures, the number of pores increased significantly (Fig. 6c), resulting in the density decrease, as shown in Fig. 6(d). The theoretical density of the AlSi10Mg alloy was 2.68 g/cm^3, and the relative density of the as-fabricated samples was ~99.7%. The mean value of the density of the aged specimens gradually decreased from ~98.4% (130 °C) to ~97.9% (190 °C). From the statistical results (Fig. 6(e)), the growth of pores was mainly

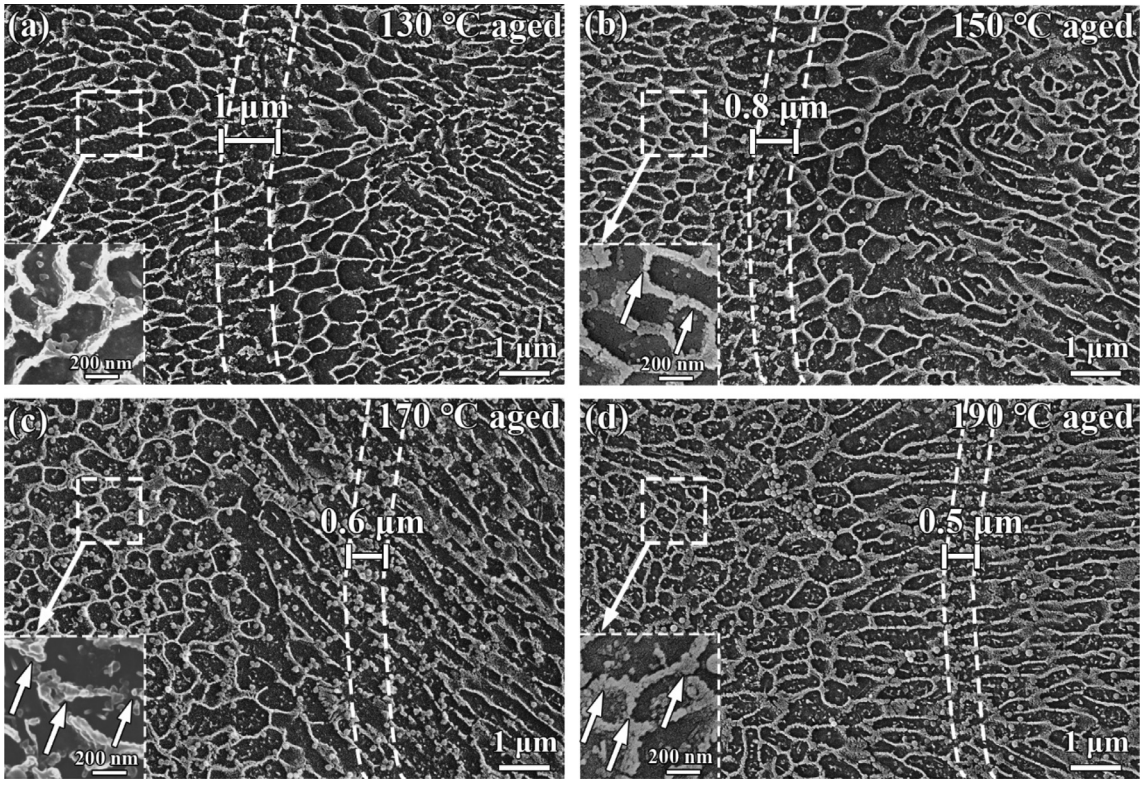

Fig. 5. Fine cell structures after aging at (a) 130 °C, (b) 150 °C, (c) 170 °C and (d) 190 °C.

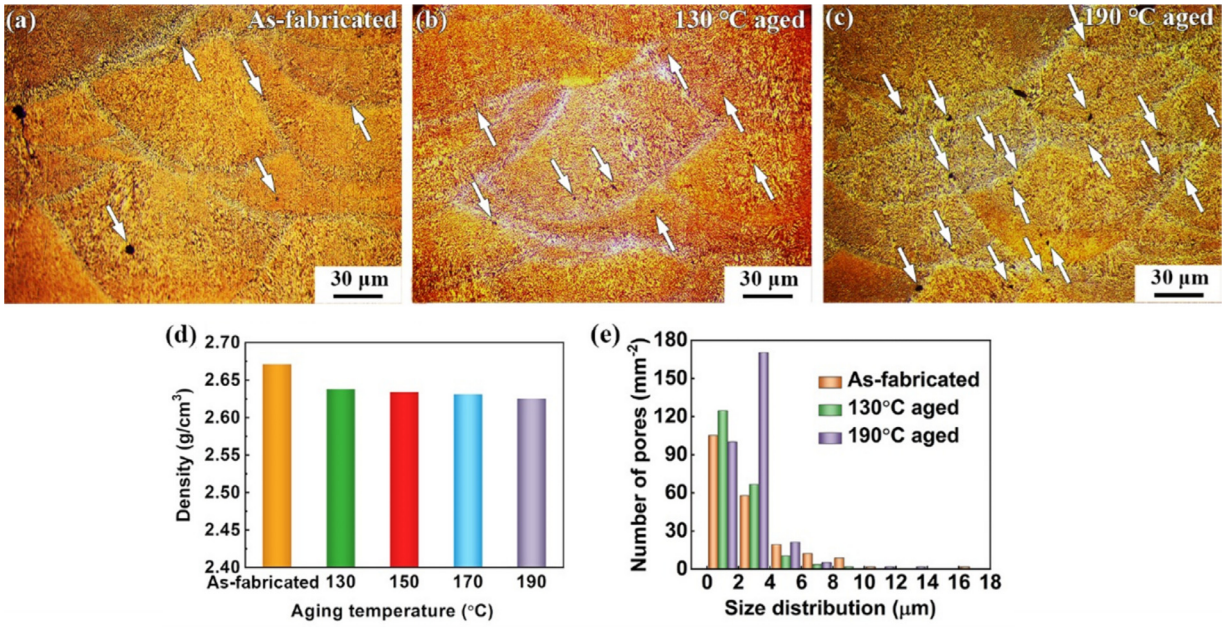

Fig. 6. Defect distribution of (a) as-fabricated and (b, c) aged samples, (d) density of as-fabricated and aged samples (arrows indicate pore defects), (e) number and size distribution of pores.

concentrated on the small pores less than 4 μm, the 190 °C aged sample showed the most obvious growth trend.

As shown in Fig. 7, the pores exhibited two kinds of morphologies. The type I pores were irregular (Fig. 7(a)), which formed during the SLM process. The type I pores were usually observed around the oxides and in the center of the molten pool, where high recoil pressure and Marangoni effect were involved. The type II pores were relatively small (< 10 μm) and usually exhibited a regular shape (Fig. 7(b) and (c)). Most of the type II pores were distributed near the inner border of the molten pool and they grew up after a higher temperature aging (Fig. 7(c)).

3.1.3. Grain size

Fig. 8(a) shows the microstructure of the as-fabricated sample characterized by EBSD. According to the grain size distribution, the molten pool could be divided into two zones, i.e., small equiaxed grains in the HAZ, and elongated columnar grains in the molten pool. The size of the equiaxed grains was ~1 μm, while the size of

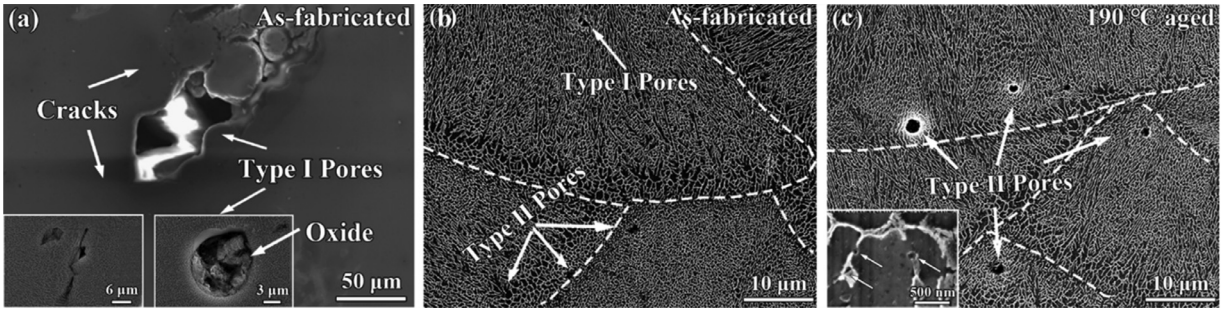

Fig. 7. Defect morphologies of (a, b) as-fabricated and (c) 190 °C aged samples.

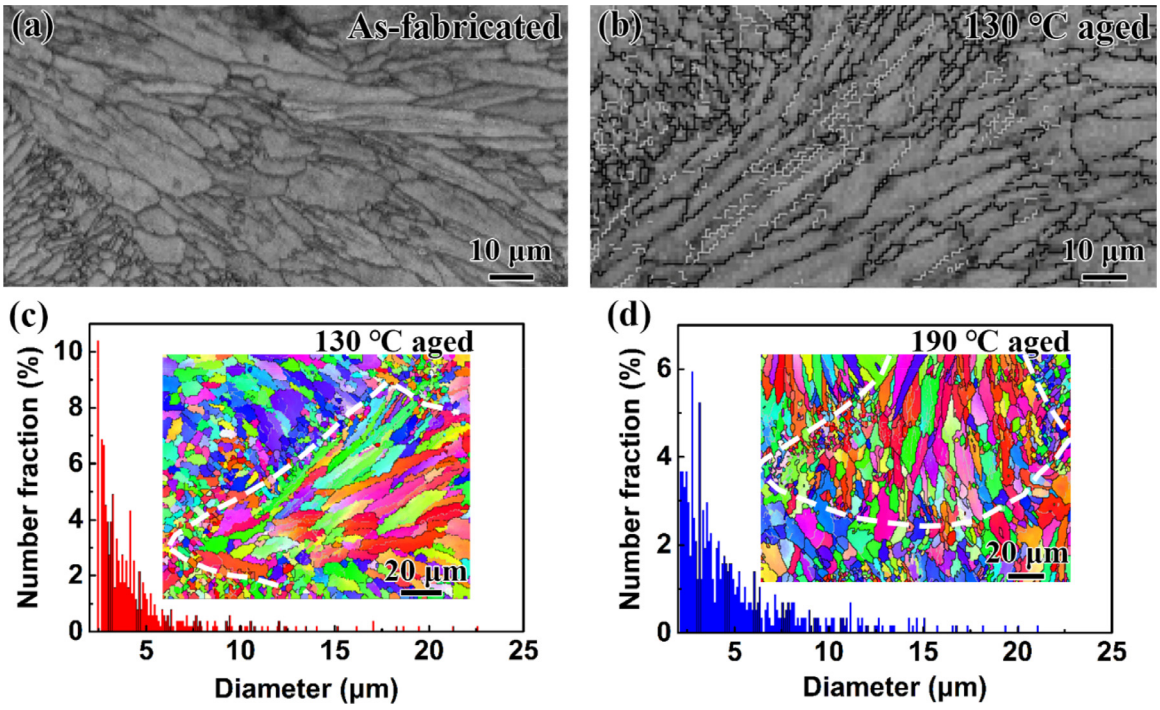

Fig. 8. Microstructure of (a) as-fabricated sample and (b) 130 °C aged sample, grain size distribution profiles of (c) 130 °C aged sample and (d) 190 °C aged sample.

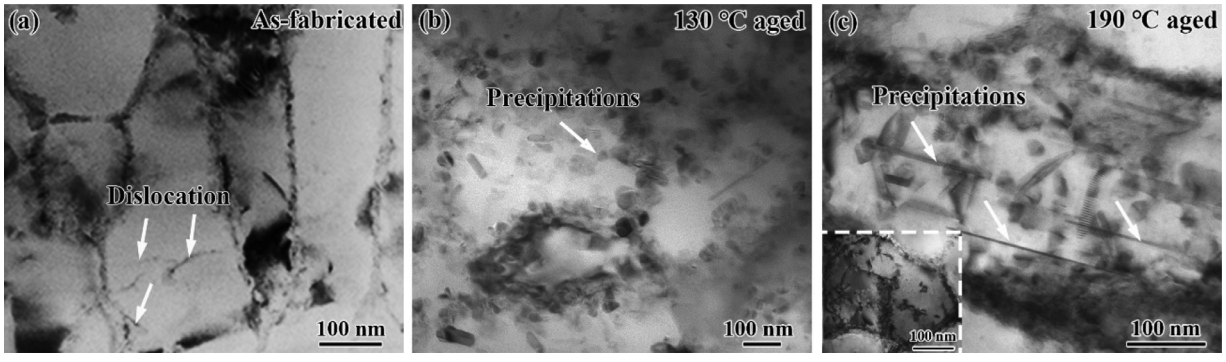

Fig. 9. TEM images showing precipitates in (a) as-fabricated sample, (b) 130 °C aged sample, and (c) 190 °C aged sample.

columnar grains was ~10 μm. It should be noted that, after low temperature aging at 130 °C, no obvious grain growth was observed (Fig. 8(b) and (c)). However, with elevated aging temperature, the average grain size was slightly increased from 4.1 μm (as-fabricated) to 4.9 μm (190 °C aged), as shown in Fig. 8(d).

3.1.4. Phases

For the as-fabricated sample, cell structure with few rod-like particles could be observed in Fig. 9(a). As the aging temperature increased, the precipitates with different shapes gradually formed. Massive rod-like precipitates with a length of ~50 nm were homogeneously distributed within the cells after aging at 130 °C (Fig. 9(b)). With increased aging temperature, a large number of precipitations were observed (Fig. 9(c)).

STEM images, high-angle annular dark-field images (HAADF) and the corresponding fast Fourier transform (FFT) pattern are shown in Fig. 10. As can be observed in EDS mappings (Fig. 10(a)), high content of Si element was detected in the spherical and

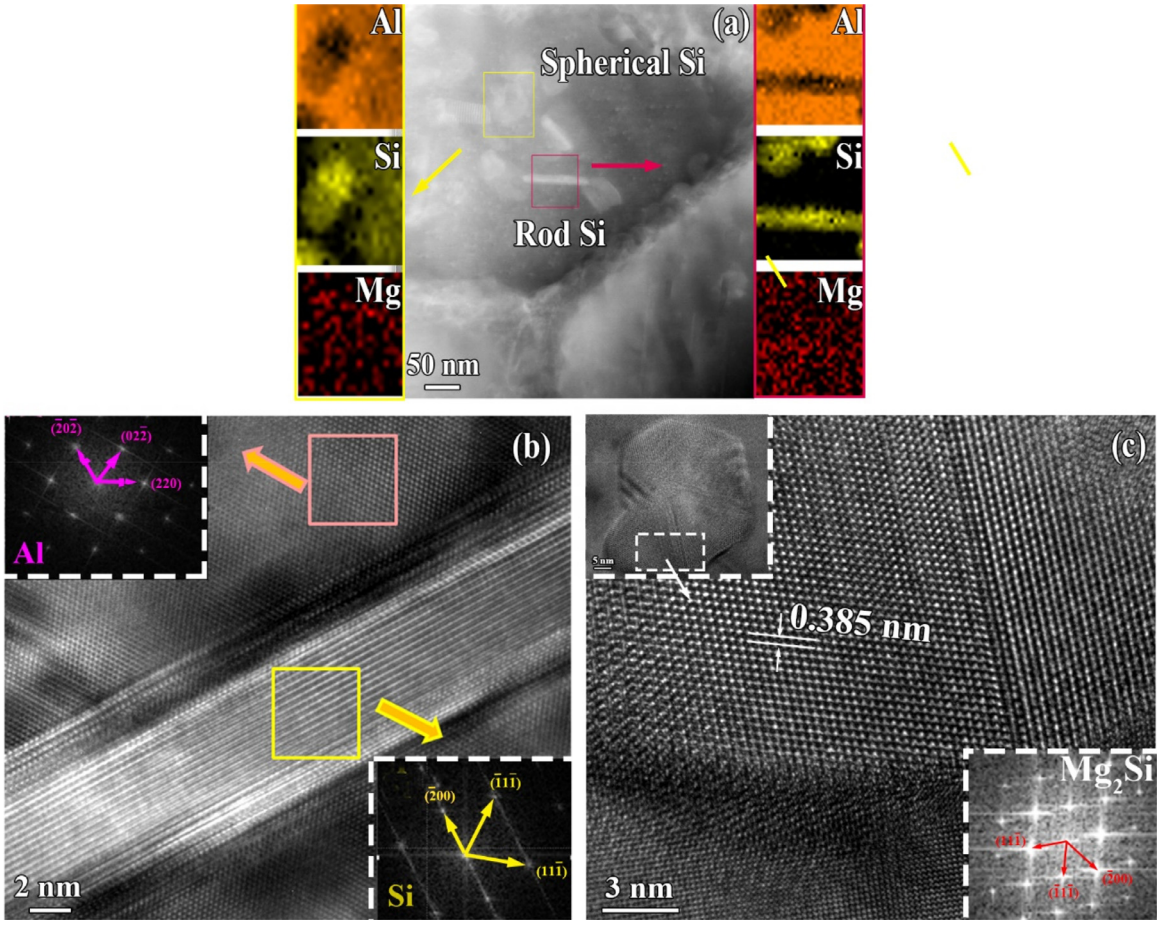

Fig. 10. (a) STEM images of precipitates inside the cells and (b, c) HAADF images of rod-like Si and Mg_2Si of 190 °C aged sample.

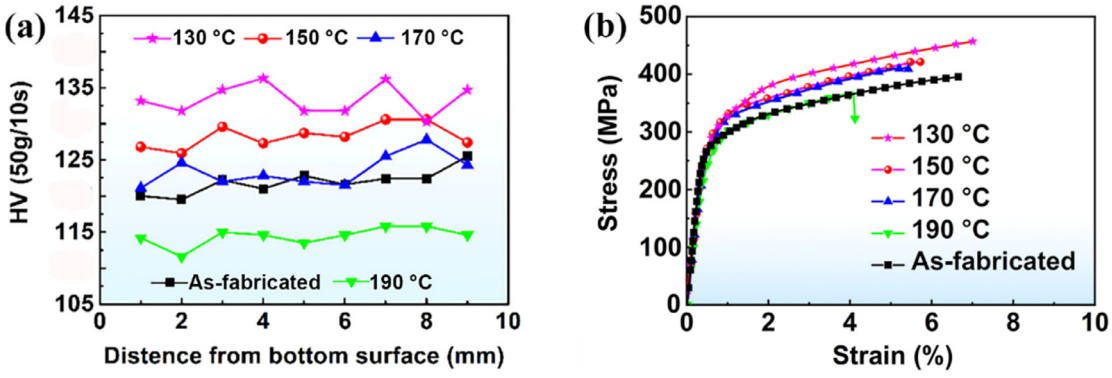

Fig. 11. (a) Hardness distribution profiles and (b) tensile curves of as-fabricated and aged samples.

rod nano-precipitates. Furthermore, the Si particles had a semi-coherent interface with the Al matrix, as confirmed by the HAADF and FFT pattern in Fig. 10(b). Some irregular particles were identified as Mg_2Si [34], as shown in Fig. 10(c).

3.2. Mechanical properties

Fig. 11(a) reveals that the average microhardness of the as-fabricated sample was 121.93 ± 1.65 HV along the building direction. After aging at 130 °C, the hardness increased to 133.42 ± 2.03 HV, which was 10% higher than that of the as-fabricated sample. However, with further increased aging temperature, the microhardness significantly decreased.

As indicated in Fig. 11(b), the as-fabricated sample showed an ultimate tensile strength (UTS) of 402.83 MPa, with an elongation (EL) of 6.37% along the building direction. After low temperature aging, exciting results were obtained (Table 2). For 130 °C aged sample, the strength improved significantly. The UTS and EL increased to 451.02 MPa and 6.46%, respectively. Clearly, with optimized aging treatment, the shortcomings in the mechanical properties of the SLM samples along the building direction were overcome. With further increase in aging tempertature from 150 °C to 190 °C, the comprehensive mechanical properties decreased gradually.

The fracture morphologies of the as-fabricated and aged samples are shown in Fig. 12. As revealed in Fig. 12(a), cracks formed

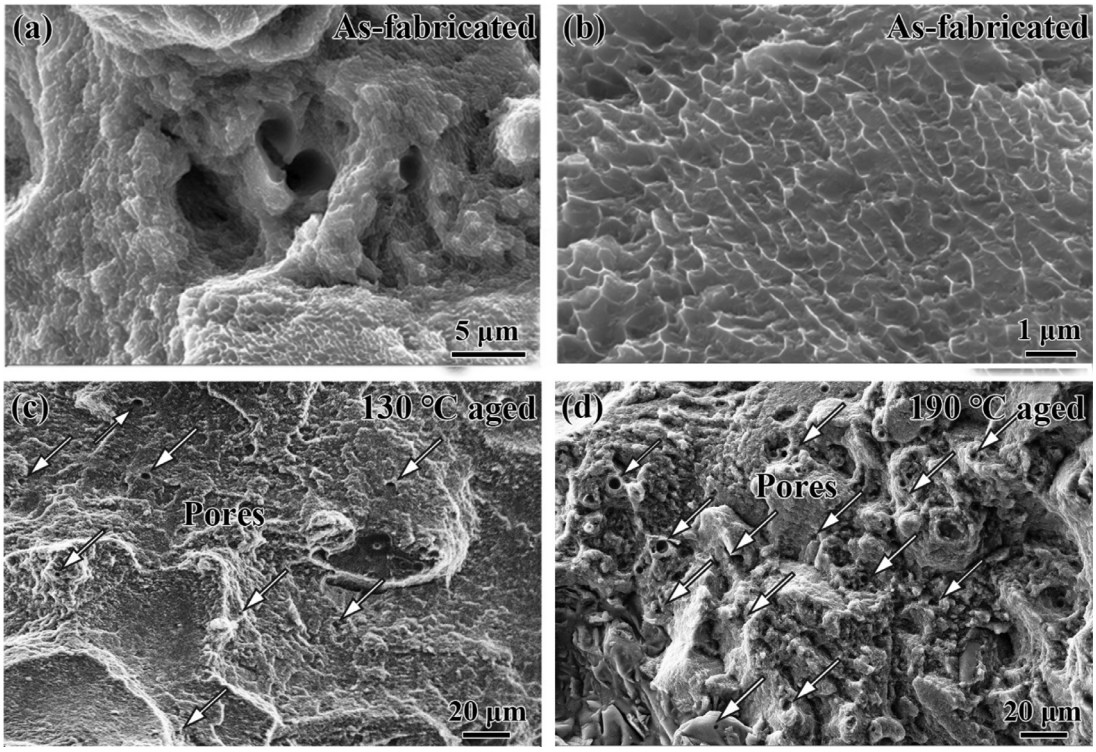

Fig. 12. Fracture morphologies of (a, b) as-fabricated samples and (c, d) aged samples, the arrows indicate pores observed on the fracture surface.

Table 2
UTS and EL of as-fabricated and aged samples along building direction.

Processing	YS, MPa	UTS, MPa	EL,%
As fabricated	276 ± 6	403 ± 6	6.37 ± 0.23
130 °C aged	309 ± 1	451 ± 10	6.46 ± 0.43
150 °C aged	296 ± 4	433 ± 13	5.30 ± 1.82
170 °C aged	293 ± 11	408 ± 9	3.18 ± 0.38
190 °C aged	270 ± 14	380 ± 34	3.54 ± 1.71

along the type I pores. Cao et al. [35] found that, irregular shape pores with sharp corner could produce stress concentration and damage mechanical properties. As shown in Fig. 12(b), the dimples of as-fabricated sample were very shallow and the dimple size was corresponding to the diameter of Si network structure. In Fig. 12(c), after aging at 130 °C, a few small pores with diameters of 2–5 μm could be found. These pores had the same morphology with the type II pores in Fig. 7. As indicated in Fig. 12(d), for 190 °C aged sample, many type II pores were observed, the increased number of these pores resulted in lower elongation (Table 2).

4. Discussion

4.1. Formation and growth of pores

The main formation mechanism of pore defects can be summarized as follows:

Pores within powders. The SLM AlSi10Mg powders were mainly produced by gas atomization, gas pores were commonly observed inside the powders. During SLM, these defects might be “freezed” within the molten pool.

H_2O. The Al alloy powders used for SLM was easy to absorb moisture. The H_2O reacted with Al at elevated temperature, resulting in the formation of Al_2O_3, $Al(OH)_3$ and hydrogen pores. Since the solubility of hydrogen in the liquid phase was much higher than that in the solid phase, it was very easy to form hydrogen gas pores during solidification.

Oxide. Due to the poor wettability between oxide film and Al, defects such as pores and microcracks were formed around oxides.

Captured gas pores during SLM. With the unstable material flow, spatter and vapor, pores constantly appeared and disappeared in the molten pool. Due to the extremely high cooling rate, gas pores could be captured and freezed during SLM.

In this study, the location, diameter, growth tendency of the two types of pores showed major differences. The type I pores generally presented a larger diameter, and could be found in the center of the molten pool or at the boundary of two molten pools. Oxide particles and micro-cracks were commonly observed within or near the type I pores. The formation of the type I pores was highly related to the SLM parameters, which involved oxide particle formation and spatter of molten pool during SLM [33,36–38].

The small type II pores mainly formed around the inner border of the molten pool during SLM (Fig. 7(b)). With higher aging temperature, some of the small type II pores (< 4 μm) grew gradually (Fig. 7(c)), which should be caused by the release of hydrogen [39]. Ghosh et al. [40] reported that, high density of pores occurred at a high cooling rate and high initial hydrogen content, resulting in reduced UTS and EL, especially for the UTS. Compared with that of the type I pores, the surfaces of the type II pores were smooth and free of broken oxides, as shown in Fig. 7(c).

It has been reported that the residual stress near the inner border of the molten pool was very high [41,42]. This phenomenon was caused by the extremely high temperature gradient during SLM. According to the simulation results, the temperature at the center of molten pool exceeded 1400 °C [43], while the temperature in the HAZ was about 600 °C [41]. Due to the small size of the molten pool (~100 μm), the temperature gradient could be as high as 10^6–10^7 K/m [44,45]. The cooling rate gradually in-

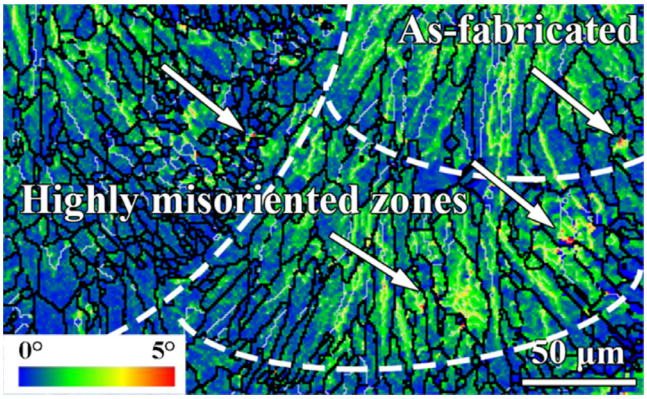

Fig. 13. KAM maps of as-fabricated sample.

creased as the distance from the center of the molten pool increased [33,41]. Therefore, the inner border near the HAZ exhibited the highest cooling rate, resulting in high misorientation within grains (Fig. 13). The diffusion and release of hydrogen were accelerated in these highly misoriented zones [46], the increased pressure within the small pores caused their repaid growth at elevated temperature.

4.2. Microstructure evolution during heat treatment

Grain growth and phase precipitation were sensitive to the heat treatment temperature and holding time [20]. The changes in the precipitate morphologies, cell diameter, and homogenized HAZ could be explained by the thermally activated solid-state diffusion of Si element [47]. Supersaturated solid solution microstructure was formed due to the rapid solidification of the molten pool [29,48]. After aging, a large number of spherical and rod-like Si gradually precipitated (Fig. 9(b) and (c)). At higher aging temperature, the Si precipitates significantly coarsened and connected due to the accelerated diffusion, therefore, more cells were formed (Fig. 5). As a result, the mean diameter of the cells after aging decreased from 0.75 μm (130 °C) to 0.34 μm (190 °C), as shown in Fig. 5(a) and (d). The precipitation of Si in the HAZ was also accelerated at elevated aging temperature, with the formation of fine Si network, the width of broken Si network in the HAZ decreased from 1.8 μm to 0.5 μm (Figs. 4d and 5).

According to the above discussion, the microstructural evolution of SLM AlSi10Mg sample at elevated aging temperatures is schematically illustrated in Fig. 14. The laser beam heated up the raw powders with remarkably high speed, small molten pool with extremely high temperature gradient formed. Due to the unstable material flow, recoil pressure and the presence of moisture, two types of pores formed during solidification, and highly misoriented zones formed along the inner border of the molten pool. With the elevated aging temperature from 130 °C to 190 °C, Si phase gradually precipitated, resulting in coarsened Si network, refined cells, and homogenized HAZ. The small type II pores grew within the highly misoriented zones.

4.3. Mechanical property improvements

Compared with the as-fabricated sample, the mechanical properties along the building direction of 130 °C aged sample improved significantly (Table 2). With the elimination of the weak zone and anisotropy in the mechanical properties, the reliability of SLM parts could be exceedingly enhanced. The significantly improved strength for the aged SLM samples could be attributed to following two factors.

Firstly, after 130 °C aging treatment, the total area of Si network increased from 32.6 to 37.2%, the diameter of cells and the width of broken Si network in the HAZ decreased significantly (Fig. 5), resulting in a more homogeneous microstructure. It could be deduced from Fig. 9(b) that, due to the further precipitation of Si particles within the cells, the movement of dislocations would be hindered, leading to higher strength. The fracture surface of the as-fabricated sample was very smooth, as can be clearly observed in Fig. 15(a). According to the results of Takata et al. [20], the broken

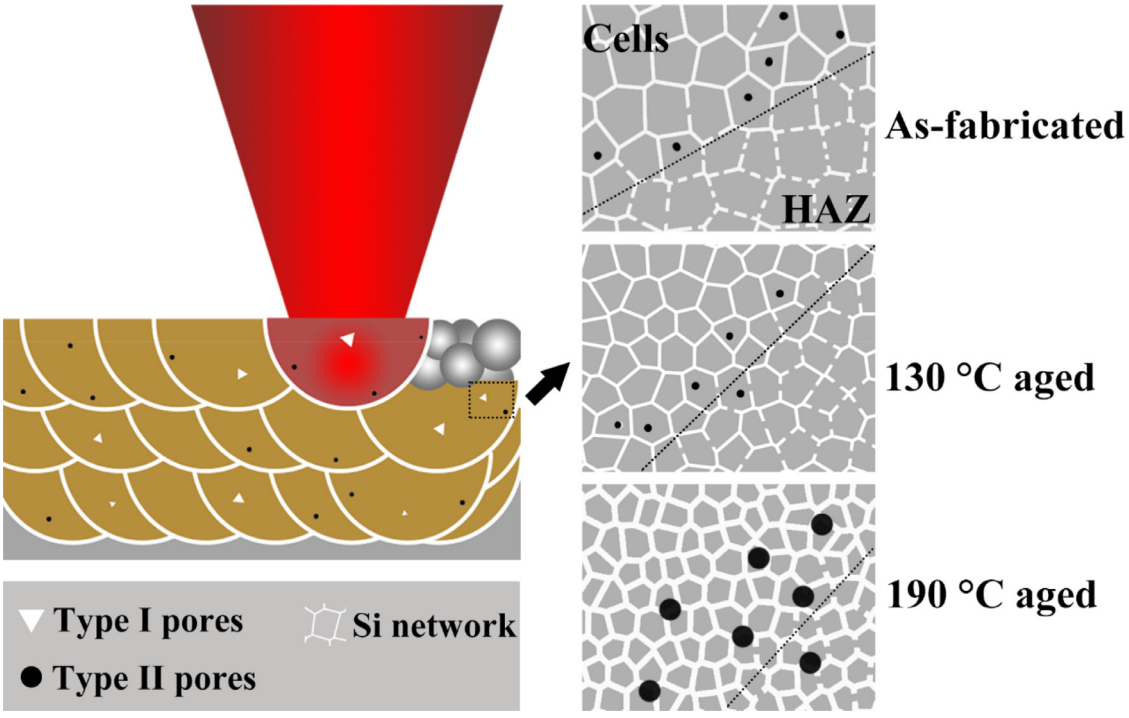

Fig. 14. Illustration of microstructural evolution during SLM and subsequent aging.

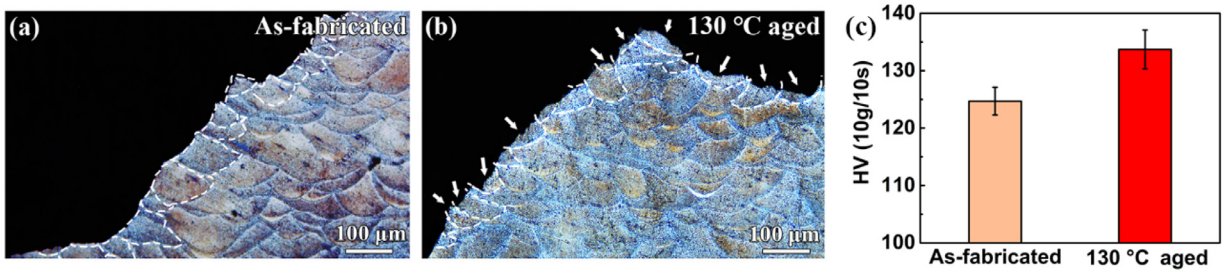

Fig. 15. Crack propagation path of (a) as-fabricated and (b) 130 °C aged samples, (c) hardness near molten pool boundaries (the arrows indicate crack propagation through the molten pools).

Si particles along the HAZ had negative effects on the ductility of SLM sample. During tensile deformation, cracks formed near these brittle particles, and caused fracture along the HAZ at early stage. In our study, with the further precipitation of Si after direct aging, the hardness near the border of the molten pool increased (Fig. 15(c)), the local deformation was alleviated, and the crack travelled through the molten pools (as pointed out in Fig. 15(b)), led to higher strength and elongation of the aged samples. However, with further decreasing aging temperature to 80 °C, the hardness of 80 °C × 4 h aged sample (121.20 ± 0.99 HV) was very close to that of the as-fabricated sample (121.93 ± 1.65 HV), due to the low precipitation rate of Si phase at low temperature. It can be inferred that to achieve improved hardness and strength, the aging time at 80 °C should be significantly extended. It is not desirable for practical application.

Secondly, with low temperature aging at 130 °C, the number of defects could be controlled at a relatively low level. As shown in Fig. 5, with the increase of aging temperature, finer cell structure was obtained, which should result in higher hardness and strength. However, a large number of small gas pores apperared after aging at 190 °C, resulting in decreased density (from 99.7% to 97.9%). Therefore, the mechanical properties of directly aged sample were dominated by the competition between microstructural optimization and internal defect growth. In this study, direct aging at 130 °C was determined as the optimized heat treatment method for SLM AlSi10Mg samples.

5. Conclusions

In this study, aiming at improving the mechanical properties of SLM AlSi10Mg samples along the building direction, direct aging at various temperatures was introduced. The microstructural evolution as well as the formation mechanism of defects were investigated. The following conclusions can be drawn.

(1) With increasing the aging temperature from 130 to 190 °C, Si phase precipitated gradually, forming finer cell structure and homogenized heat affected zone (HAZ). Furthermore, no obvious grain growth was observed after aging treatment.
(2) Two types of pores were observed in the aged samples: the type I pores with oxide inside, and the type II pores along the inner border of the molten pool. With increasing aging temperature, significant growth of type II pores occurred, which was highly related to the formation of highly misoriented zones, reducing the density of the samples.
(3) Balancing the refinement of cell structure and growth of defects, 130 °C was determined as the optimized aging temperature. Compared with the as-fabricated sample, 130 °C directly aged sample showed significantly improved tensile strength along the building direction (from 403 MPa to 451 MPa), with a relatively high elongation of 6.5%.

Declaration of Competing Interest

The authors declare that they have no known competing financial interests or personal relationships that could have appeared to influence the work reported in this paper.

CRediT authorship contribution statement

H. Zhang: Conceptualization, Investigation, Writing – original draft. **Y. Wang:** Methodology, Investigation. **J.J. Wang:** Formal analysis, Validation. **D.R. Ni:** Resources, Project administration. **D. Wang:** Data curation, Resources. **B.L. Xiao:** Writing – review & editing, Funding acquisition. **Z.Y. Ma:** Supervision, Writing – review & editing.

Acknowledgments

This work was financially supported by the National Key R&D Program of China (No. 2017YFB0703104). The authors would like to thank J.L. Zhao (Renishaw plc) for kindly providing guidance for SLM parameter optimizing.

References

[1] J.H. Martin, B.D. Yahata, J.M. Hundley, J.A. Mayer, T.A. Schaedler, T.M. Pollock, Nature 549 (2017) 365–369.
[2] A. Hadadzadeh, B.S. Amirkhiz, S. Shakerin, J. Kelly, J. Li, M. Mohammadi, Addit. Manuf. 31 (2020) 100937.
[3] L. Yan, Y. Chen, F. Liou, Addit. Manuf. 31 (2020) 100901.
[4] A.G. Demir, C.A. Biffi, J. Manuf. Process. 37 (2019) 362–369.
[5] Q. Yan, B. Song, Y. Shi, J. Mater. Sci. Technol. 41 (2020) 199–208.
[6] H. Tan, D. Hao, K. Al-Hamdani, F. Zhang, Z. Xu, A.T. Clare, Mater. Lett. 214 (2018) 123–126.
[7] N.O. Larrosa, W. Wang, N. Read, M.H. Loretto, C. Evans, J. Carr, U. Tradowsky, M.M. Attallah, P.J. Withers, Theor. Appl. Fract. Mech. 98 (2018) 123–133.
[8] J. YU, W. Jing, N.I. Dingrui, X.I.A.O. Bolv, M.A. Zongyi, P.A.N. Xinglong, Acta Metall. Sin. 54 (2018) 1725–1734.
[9] L. Zhuo, Z. Wang, H. Zhang, E. Yin, Y. Wang, T. Xu, C. Li, Mater. Lett. 234 (2019) 196–200.
[10] Y. Cao, X. Lin, Q.Z. Wang, S.Q. Shi, L. Ma, N. Kang, W.D. Huang, J. Mater. Sci. Technol 62 (2021) 162–172.
[11] J. Bi, Z. Lei, Y. Chen, X. Chen, N. Lu, Z. Tian, X. Qin, J. Mater. Sci. Technol. 67 (2021) 23–35.
[12] A. Heinz, A. Haszler, C. Keidel, S. Moldenhauer, R. Benedictus, W.S. Miller, Mater. Sci. Eng. A (2000) 102–107.
[13] F. Calignano, Mater. Des. 64 (2014) 203–213.
[14] L. Thijs, K. Kempen, J.P. Kruth, J. Van Humbeeck, Acta Mater. 61 (2013) 1809–1819.
[15] D. Manfredi, F. Calignano, M. Krishnan, R. Canali, E. Ambrosio, E. Atzeni, Mater. (Basel) 6 (2013) 856–869.
[16] D.D. Gu, W. Meiners, K. Wissenbach, R. Poprawe, Int. Mater. Rev. 57 (2013) 133–164.
[17] J.C. Williams, E.A. Starke, Acta Mater. 51 (2003) 5775–5799.
[18] G. Yu, D. Gu, D. Dai, M. Xia, C. Ma, K. Chang, Appl. Phys. A 122 (2016).
[19] K. Kempen, L. Thijs, J. Van Humbeeck, J.P. Kruth, Mater. Sci. Technol. 31 (2015) 917–923.
[20] N. Takata, H. Kodaira, K. Sekizawa, A. Suzuki, M. Kobashi, Mater. Sci. Eng. A 704 (2017) 218–228.
[21] R. Casati, M. Hamidi Nasab, M. Coduri, V. Tirelli, M. Vedani, Met. Basel 8 (2018) 954.
[22] I. Rosenthal, R. Shneck, A. Stern, Mater. Sci. Eng. A 729 (2018) 310–322.

[23] Q. Han, Y. Jiao, Int. J. Adv. Manuf. Technol. 102 (2019) 3315–3324.
[24] L.F. Wang, J. Sun, X.L. Yu, Y. Shi, X.G. Zhu, L.Y. Cheng, H.H. Liang, B. Yan, L.J. Guo, Mater. Sci. Eng. A 734 (2018) 299–310.
[25] W. Li, S. Li, J. Liu, A. Zhang, Y. Zhou, Q. Wei, C. Yan, Y. Shi, Mater. Sci. Eng. A 663 (2016) 116–125.
[26] A.H. Maamoun, M. Elbestawi, G.K. Dosbaeva, S.C. Veldhuis, Addit. Manuf. 21 (2018) 234–247.
[27] Y. Kaibin, L. Yunzhong, Y. Changyi, Mater. Sci. Eng. Powder Metall. 23 (2019) 298–305.
[28] Y. Wang, J.J. Wang, H. Zhang, H.B. Zhao, D.R. Ni, B.L. Xiao, Z.Y. Ma, Acta Metall. Sin. 57 (2021) 613–622.
[29] M. Das, V.K. Balla, D. Basu, S. Bose, A. Bandyopadhyay, Scr. Mater. 63 (2010) 438–441.
[30] J. Fiocchi, A. Tuissi, P. Bassani, C.A. Biffi, J. Alloys Compd. 695 (2017) 3402–3409.
[31] J. Delahaye, J.T. Tchuindjang, J. Lecomtebeckers, O. Rigo, A. Habraken, A. Mertens, Acta Mater. 175 (2019) 160–170.
[32] E.A. Jägle, Z. Sheng, L. Wu, L. Lu, J. Risse, A. Weisheit, D. Raabe, JOM 68 (2016) 943–949.
[33] J. Zhang, B. Song, Q. Wei, D. Bourell, Y. Shi, J. Mater. Sci. Technol. 35 (2019) 270–284.
[34] A. Hadadzadeh, B.S. Amirkhiz, M. Mohammadi, Mater. Sci. Eng. A 739 (2019) 295–300.
[35] H. Cao, M. Hao, C. Shen, P. Liang, Vacuum 146 (2017) 278–281.
[36] J.H. Tan, W.L.E. Wong, K.W. Dalgarno, Addit. Manuf. 18 (2017) 228–255.
[37] M. Tang, P.C. Pistorius, Int. J. Fatigue 94 (2017) 192–201.
[38] N.T. Aboulkhair, N.M. Everitt, I. Ashcroft, C. Tuck, Addit. Manuf. 1-4 (2014) 77–86.
[39] X.P. Li, K.M. O'Donnell, T.B. Sercombe, Addit Manuf 10 (2016) 10–14.
[40] I. Ghosh, S.K. Das, N. Chakraborty, Neural Comput. Appl. 25 (2013) 653–662.
[41] Y. Li, D. Gu, Mater. Des. 63 (2014) 856–867.
[42] Z.H. Xiong, S.L. Liu, S.F. Li, Y. Shi, Y.F. Yang, R.D.K. Misra, Mater. Sci. Eng. A 740-741 (2019) 148–156.
[43] X.P. Li, X.J. Wang, M. Saunders, A. Suvorova, L.C. Zhang, Y.J. Liu, M.H. Fang, Z.H. Huang, T.B. Sercombe, Acta Mater. 95 (2015) 74–82.
[44] D. Gu, Q. Shi, K. Lin, L. Xi, Addit. Manuf. 22 (2018) 265–278.
[45] Y. Huang, L. Yang, X. Du, Y. Yang, Int. J. Therm. Sci. 104 (2016) 146–157.
[46] J. Albrecht, I.M. Bernstein, A.W. Thompson, Metall. Trans. A 13 (1982) 811–820.
[47] J. Delahaye, J.T. Tchuindjang, J. Lecomte-Beckers, O. Rigo, A.M. Habraken, A. Mertens, Acta Mater. 175 (2019) 160–170.
[48] N. Takata, M. Liu, H. Kodaira, A. Suzuki, M. Kobashi, Addit. Manuf. 33 (2020) 101152.